

Temporal optimization of Lagrangian perturbation schemes

Georgios Karakatsanis^{1,4}, Thomas Buchert² and Adrian L. Melott³

¹ Max-Planck-Institut für Astrophysik, Postfach 1523, D-85740 Garching, Germany

² Theoretische Physik, Ludwig-Maximilians-Universität, Theresienstr. 37, D-80333 München, Germany

³ Department of Physics and Astronomy, University of Kansas, Lawrence, KS 66045, U.S.A.

⁴ National Observatory of Athens, Lofos Nimfon, Thessio, 18115 Athens, Greece

Received ????, accepted ????

Abstract. The Lagrangian perturbation theory on Friedmann-Lemaître cosmologies is compared with numerical simulations (tree-, adaptive P³M- and PM codes). In previous work we have probed the large-scale performance of the Lagrangian perturbation solutions up to the third order by studying their cross-correlations with N-body simulations for various power spectra (Buchert *et al.* 1994, Melott *et al.* 1995, Weiß *et al.* 1996). Thereby, spatial optimization techniques were applied by (high-frequency-)filtering of the initial power spectra. In this work the novel method of temporal optimization [Shifted-Time-Approximation (STA) and Frozen-Time-Approximation (FTA)] is investigated and used. The method is designed to compensate the native property of Lagrangian perturbation solutions to delay the collapse of structures. The method can be treated analytically. Applying the STA and FTA prescriptions a significant improvement of the performance of Lagrangian perturbation schemes up to r.m.s density contrast of about 10 (as measured by cross-correlation, relative phase error and power-spectrum statistics) is observed. Using this tool we investigate a local study of special clustering models of dark matter as candidates for typical elements of the large-scale structure in the Universe, and so also focus on the performance of the perturbation solutions on smaller scales at high-spatial resolution. The models analyzed were presented in (Buchert *et al.* 1996) and allow studying typical features of the clustering process in the non-linear regime. The spatial and temporal limits of applicability of the solutions at second and third order are determined and compared with the first-order solution, which is equivalent to the “Zel’dovich approximation” (Zel’dovich 1970, 1973) for the type of initial data analyzed.

Key words: Gravitation; Instabilities; Methods: analytical; Cosmology: theory; large-scale structure of Universe

1. Introduction

It is generally appreciated that Lagrangian perturbation theory provides successful models of large-scale structure down to the scale where the density field becomes non-linear (the r.m.s. density contrast is of order unity) (Kofman *et al.* 1992, Coles *et al.* 1993, Melott *et al.* 1994, Buchert *et al.* 1994, Bouchet *et*

al. 1995). For models with considerable small-scale power the truncation of high-frequency components in the initial fluctuation spectrum allows application of the Lagrangian schemes down to galaxy group mass scales as was found for a family of power-law hierarchical models (Melott *et al.* 1994, 1995). The Lagrangian schemes are most suitable tools in the regime where the spectral index is negative on small scales. In the case where the truncation scale in the initial spectrum corresponds to the Nyquist frequency of a N-body simulation there is no need for N-body computing. There is agreement about the fact that Lagrangian schemes can replace N-body integrators above some scale close to, but smaller than the non-linearity scale; they provide fast and effective one-time step mappings applicable to various kinds of studies of hierarchical cosmologies (such as CDM models, Weiß *et al.* 1996) and statistical studies of, e.g., the modeling of pencilbeams at high resolution (Weiß & Buchert 1993), or the distribution of clusters (Borgani *et al.* 1995). In the previously mentioned works the decreasing performance of the spatially optimized Lagrangian schemes at nonlinear scales and, of course, near the epoch of shell-crossing has been pointed out. Here we show the possibility to overcome this problem and to maintain a good performance until the epoch of caustic formation by employing a temporal optimization method (Shifted-Time-Approximation). Further we suggest to extend the usability of the Lagrangian perturbation theory to even later stages where the Lagrangian theory is not formally valid using the Frozen-Time-Approximation.

The statement of applicability of the Lagrangian approximations in previous works is made on the basis of cross-correlation statistics of density fields in which the internal substructures are not resolved. We here also address the question whether these approximations can model these substructures. Since analytical models are much faster to execute, it is our goal to understand whether and how these substructures compare with those of N-body simulations. Here, we should be able to learn more about the details of the clustering process, but also about the problems which are inherent in a Lagrangian perturbation approach. With this work we want to approach the limits of Lagrangian perturbation schemes by means of studying special initial data which are suitable to process these questions efficiently.

On one hand we have taken various numerical N-body integrators to assure that the features we want to compare with do not depend on whether we use a tree-code, an adaptive P³M-

Send offprint requests to: G. Karakatsanis

code, or a PM-code. Previous comparisons have only been performed with PM-codes. On the other hand we are interested in both the local details of structure formation and the statistical properties of the overall distribution, which have been tested in previous work for (physically) larger simulation boxes.

2. Clustering models, N-body integrators and cross-correlation statistics

2.1. Clustering models

We start with the analysis of a simple plane-wave model (Model I) as described by Buchert *et al.* (1996). We stick to that model first since, despite its simplicity, it already shows the principal features of gravitational collapse we are interested in. Details about the construction of this model are given in the appendix of Buchert *et al.* (1996). Also in other work on related subjects this model is useful as an example (Mo & Buchert 1990, Matarrese *et al.* 1992), or as a toy-model for the comparison of different approximation schemes.

We then move to a generic model (Model II), i.e., a model without symmetry, but restricted to a small enough box to assure the resolution of patterns we are interested in. The construction and the properties of this model are also described in (Buchert *et al.* 1996). In both the special and the generic model we quantitatively investigate the delay of collapse times in the Lagrangian schemes compared with the collapse time of the numerically simulated structures, and express this delay in terms of the r.m.s. density fluctuation of structures or the spatial scale, respectively.

2.2. N-body integrators

We use a hierarchical tree-code (Bouchet & Hernquist 1988) with incorporated periodic boundary conditions based on the Ewald method (Hernquist *et al.* 1991) as well as the adaptive P³M-code by Couchman (1991), which is also used as a standard PM-code as described in (Couchman 1991).

The simulations have been done for 64³ particles and the standard choices for the tolerance parameter 0.75, softening-length 0.015 and time-step 0.2 in the tree-code (Suginohara & Suto, priv.comm., Suginohara *et al.* 1991). For the P³M- and the PM code the settings are according to the work of Efstathiou *et al.* (1985). Grid spacing for the PM simulations and initially for P³M was 128³. The parameter settings used have been tested on the exact plane-symmetric model to yield the same collapse time.

2.3. The statistics used

We use three different statistical methods. Firstly, the cross-correlation coefficient S to compare the resulting density fields,

$$S := \frac{\langle \delta_1 \delta_2 \rangle}{\sigma_1 \sigma_2}, \quad (1)$$

where $\delta_\ell, \ell = 1, 2$ represent the r.m.s. density contrasts in the analytical and the numerical approximations, respectively, $\sigma_\ell = \sqrt{\langle \delta_\ell^2 \rangle - \langle \delta_\ell \rangle^2}$ is the standard deviation in a Gaussian random field; averages $\langle \dots \rangle$ are taken over the entire distribution. We will plot S as a function of σ_2 for different Gaussian smoothing lengths.

We believe this is the most important statistical test, because it measures whether the approximation is moving mass to the right place, with an emphasis on dense regions. (We plan to address bulk flows in underdense regions in a future study.) We allow for small errors by presenting S for the two density arrays smoothed at a variety of smoothing lengths. The correlation coefficient obeys the bound $|S| \leq 1$; $S = 1$ implies that $\delta_1 = C\delta_2$, with C constant.

Secondly, the power spectrum of the evolved N-body model and the analytical approximations were calculated and plotted against the wave number $k := |\mathbf{k}|$.

Thirdly, the phase angle accuracy is measured and displayed by $\langle \cos \theta \rangle_k$, where $\theta = \phi_1 - \phi_2$ is the difference in the phase angle of the Fourier coefficients of mass density between the approximation and the simulation. We present the results on the relative phase errors in terms of $\cos(\theta)$ as a function of k (calculated in spherical shells in k -space). Perfect agreement between the N-body result and the analytical scheme implies $\cos(\theta) = 1$, anti-correlated phases have $\cos(\theta) = -1$, and for randomized phases $\cos(\theta)$ would average to 0.

For further details on these statistics we refer the reader to Melott *et al.* (1994) and Buchert *et al.* (1994).

3. Results and Discussion

3.1. Comparison between different numerical integrators

In Fig.1a we present a comparison of the density fields at three evolution stages as predicted by the tree-code, the adaptive P³M-code and the PM-code for Model I. Since the coincidence of all three algorithms is excellent (the cross correlation coefficient lies between 0.95 and 1.00 and the relative phase error between 0.7 and 1.00), we henceforth stick to the adaptive P³M-code, which is about 2 times faster than the tree-code and has a significantly higher force resolution – due to the mesh refinement at dense regions – than the faster PM-code. This does, however, not imply that AP³M is more accurate than PM (see Suisalu & Saar 1996, Melott *et al.* 1996). In Fig.1b some statistics of this comparison are displayed.

3.2. The temporal optimization methods

Various works on the comparison of the Lagrangian perturbation theory with numerical simulations (Melott *et al.* 1994, Buchert *et al.* 1994, Munshi *et al.* 1994, Bouchet *et al.* 1995) show an improvement of the performance of the Lagrangian perturbation theory using the second-order scheme independent of the initial conditions and the fluctuation scale. This fact concerns not only the spatial accuracy mirrored in the cross-correlations, but also the time accuracy concerning the collapse time as compared with the numerical simulations. We are led to the conclusion that the spatial accuracy is also a consequence of the time evolution accuracy. The collapse time accuracy of the Lagrangian schemes increases with increasing order until the epoch of shell crossing. The time coefficients of the Lagrangian theory grow proportional to a^n for a given order n . This also means that the higher the order the earlier the break down of the theory (“blow-up effect”). During this work we indeed observed that time-shifted low-order schemes produce configurations similar to those of unshifted higher-order schemes suggesting that the Lagrangian theory reproduces the

systems evolution correctly but delayed. Under the assumption that the complete perturbation series converges to the temporally (and spatially) correct solution we can thus test the hypothesis that time shifting of the available low-order schemes will mimic the higher-order effects leading to optimal results compared with numerical simulations. This means that one can compare the Lagrangian perturbation theory with numerical simulations at the same expansion factor only formally, because the evolution stages don't correspond physically.

We introduce the time-shift factors $s_n(a_{num})$ in order to quantify the amount of the time-shift for a given order n matching the numerical simulation at the expansion factor a_{num} . Formally the assumption reads:

$$a_n = a_{num} \cdot s_n(a_{num}) \text{ with} \\ s_n < s_{n-1} ; s_n > 1 ; s_\infty = 1 ; a_n \leq a_n^{crit} ,$$

a_n is the corresponding optimally shifted expansion factor for the order n , and a_n^{crit} is the expansion factor of the shell-crossing stage which can be calculated analytically.

It turns out that this method of the Shifted-Time-Approximation (STA) leads to an astonishingly good agreement between the shifted Lagrangian schemes and the numerical simulations for both models analyzed.

The optimal time-shift has been first determined by minimizing the error in the cross-correlation statistics. The analysis of the results showed that the mechanism and criterion of this optimization method is based on the r.m.s. density contrast which has to be equal (up to about 2%) to that of the numerical simulations at the corresponding stages. This is illustrated in Figure 9 (for Model I as an example), where the r.m.s. density contrast for the numerical simulation and for both the optimized and unoptimized Lagrangian schemes is plotted as a function of the smoothing scale. The mechanism of the STA is illustrated in Fig.2a in comparison with conventional methods. The optimal time-shift of the Lagrangian schemes is *unique* and is determined by the adaptation of the value of the r.m.s. density contrast to the numerical value. The error in the cross-correlation coefficient, the power-spectrum and the phase accuracy displays *distinct and unique* minima which nearly lie at the same values of a_{min} , i.e., the "optimal" time-shift predicted is quite close in all statistics. Here, it is to be mentioned that the spatial optimization done in the "truncated Zel'dovich-approximation" (TZA; Melott *et al.* 1994) is based on the cross-correlation coefficient alone. However, they found the same rank ordering for phase accuracy as for cross-correlation. Further time-shifting decreases the performance as shown in the plots of the approximation error as a function of the shift amount (Figure 5).

Turning this result around we can use the STA method independently of the numerical simulations in order to simulate analytically the structure formation process: if a value for the r.m.s. density contrast on a certain scale for the stage we want to simulate is given, then we can analytically or even graphically determine if the STA method is valid (this means if the desired value of the r.m.s. density contrast can be reached by the Lagrangian perturbation theory), and then use the more accurate order and the corresponding optimal expansion factor.

The "blow-up effect" signals the validity limit of the Lagrangian perturbation schemes and thus of the STA method: the structures built decay and the r.m.s. density contrast decreases rapidly in contrast to the numerical simulations where further shell-crossings (due to self-gravitation of multi-stream

systems) hold the structures together. So we are led to the hypothesis that the last stable configuration produced by the Lagrangian perturbation theory (just before shell-crossing) provides the structural frame for the further nonlinear evolution. It turned out that this assumption holds. It means that, in order to get reasonable results even if the Lagrangian theory is formally no longer valid, one needs to shift the Lagrangian schemes backwards to the analytically calculable expansion factor a_n^{crit} . This method we call Frozen-Time-Approximation (FTA). FTA can also be treated analytically and leads to very good results for the epochs shortly after shell-crossing where the Lagrangian perturbation theory is formally not valid. The mechanism of the FTA method – similar to the STA mechanism – is based on the minimization of the r.m.s. density contrast difference between the numerical simulations and the Lagrangian schemes. (Equality is in this case not possible due to the structure decay and the accompanying decrease of the r.m.s. density contrast.) This method is explained in Fig.2b.

3.3. Illustration of the optimization results

Both optimization methods improve significantly on the performance of the Lagrangian schemes even at stages where the r.m.s. density contrast is above 10. This is shown in Fig.3 for the cross-correlation coefficient within the framework of the STA. After the shell-crossing expansion factor, which signals the validity limit for the STA, the error increases rapidly.

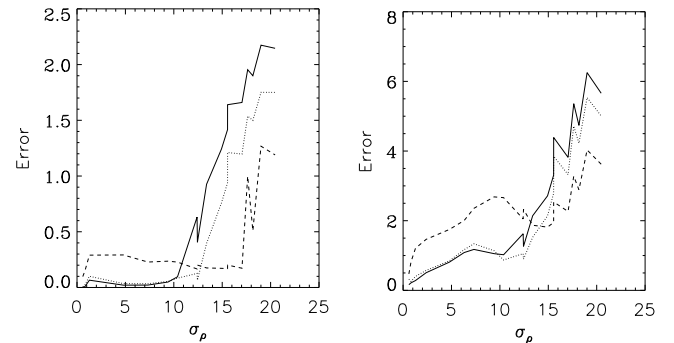


Figure 3: The absolute errors in the cross-correlation coefficient for Model I (left) and Model II (right panel) between the numerical simulation and the optimized Lagrangian schemes is shown. The 3rd-order scheme is plotted as a full line, the 2nd-order one as a dotted line and 1st-order as a dashed line.

The shell-crossing expansion factor for each order n signals the end of the validity of the STA and simultaneously the onset of the validity regime of the FTA. Thus, both methods can be combined resulting in an optimal approximation error as shown in Figs.4a,b.

Figure 6 shows the quantitative difference between the optimized and unoptimized approximation errors in all statistics used over the whole evolution sequence for Model II as an example. Figs.7–10 (some for Model I and some for Model II) further quantify the gain in performance due to the optimization technique STA by depicting the different statistics (described in Subsection 2.3). These statistics show the comparison between the Lagrangian schemes, which are evolved to the same expansion factor a_{num} as the N-body run, the N-body result itself, and the optimally time-shifted schemes for the STA technique.

The figures together with the captions are self-explanatory, so we do not present an additional discussion.

Figs. 11a,b show the approximation error from the cross correlation and relative phase error statistics resulting from the application of the FTA method for Models I and II, respectively: The approximation error is 4–5 times smaller than in the unoptimized case and reaches unique minima at the shell-crossing expansion factor. Finally, in Figure 12 we depict slices of the density field of Model I at an epoch after shell-crossing, where the unshifted and shifted Lagrangian schemes are compared with the N-body result. It is remarkable that even the first-order (Zel’dovich-)approximation displays a large gain in performance as demonstrated in Fig.12 by an increase of the maximal density contrast from 26 to 511 compared to the N-body value of 510.

4. Conclusions

We presented the novel temporal optimization methods (STA and FTA) based on native properties of the Lagrangian perturbation schemes which, combined, allow the analytical simulation of the gravitational evolution into the nonlinear regime with an optimally minimized approximation error compared with numerical simulations. We appreciate a significant gain in performance, even in the non-linear regime (up to r.m.s. density contrasts of about 10) as measured by three different statistical methods. The advantages of the temporal optimization methods are the possibility of a physical comparison between Lagrangian perturbation schemes and N-body simulations, the use of the full performance of each Lagrangian order available today, the universality of the methods (i.e., their mechanisms are only based on the variance of the approximated realization), and their analytical or even graphical treatment which is easy to put into practice.

The present results indicate that the *physical* content (concerning the spatial distribution of structure) inherent in N-body realizations does not exceed that of Lagrangian perturbation schemes up to the abovementioned stages of nonlinearity and for the given resolution limits. This could be understood in the case of convergence of the Lagrangian perturbation scheme to the solution modeled by the N-body simulation, i.e., 1. increasing the order of the perturbation scheme allows to access smaller spatial scales (in the limits we have tested), and 2. the main effect of the 4th and higher-order corrections before shell-crossing on the resolved scale can be assigned to acceleration of the collapse process which is fully compensated for by the applied temporal shift.

As in previous work we also appreciate that the second-order scheme improves on the first-order scheme (the “Zel’dovich approximation”) for both models tested and at all stages within the temporal range where the optimization techniques apply; for the third-order scheme an improvement has been detected, but this improvement is negligible at this resolution compared to the gain in performance by going to second order. This result might change by going to higher spatial resolution. However, we emphasize that the “blow-up effect”, i.e. the validity limit of the nth-order perturbation scheme imposed by its power law time dependence $\propto a(t)^n$, implies that the temporal range of validity of the schemes will decrease drastically by going to higher orders. Therefore, we expect that going to higher than 3rd order will not be useful.

Acknowledgements. We would like to thank François Bouchet, Yasushi Suto and Tatsushi Sugino-hara for useful comments and discussions and for providing us their tree-codes and Hugh Couchman for providing his adaptive P³M-code. To Gerhard Börner and Arno Weiß we are thankful for helpful discussions. GK and TB were both supported by the “Sonderforschungsbereich 375 für Astro-Teilchenphysik der Deutschen Forschungsgemeinschaft”. ALM gratefully acknowledges financial support from NASA grant NAGW3832, and the NSF EPSCoR program, as well as the use of the National Center for Supercomputing Applications.

References

- Borgani S., Plionis M., Coles P., Moscardini L., 1995, MNRAS 277, 1191
 Bouchet F.R., Hernquist L., 1988, ApJ Suppl 68, 521
 Bouchet F.R., Colombi S., Hivon E., Juszkiewicz R., 1995, Astron. Astrophys. 296, 575
 Buchert T., Melott A.L., Weiß A.G., 1994, Astron. Astrophys. 288, 349
 Buchert T., Karakatsanis G., Klaffl R., Schiller P., 1996, Astron. Astrophys., in press
 Coles P., Melott A.L., Shandarin S.F., 1993, MNRAS 260, 765
 Couchman H.M.P., 1991, Ap.J. 368, L23
 Efstathiou G., Davis M, Frenk C.S., White S.D.M. (1985), ApJ Suppl. 57, 241
 Hernquist L., Bouchet F.R., Suto Y., 1991, ApJ Suppl. 75, 231
 Kofman L.A., Pogosyan D.Yu., Shandarin S.F., Melott A.L., 1992, ApJ 393, 437
 Matarrese S., Lucchin F., Moscardini L., Saez D., 1992, MNRAS 259, 437
 Melott A.L., Pellman T., Shandarin S.F., 1994, MNRAS 269, 626
 Melott A.L., Buchert T., Weiß A.G., 1995, Astron. Astrophys. 294, 345
 Melott A.L., Splinter R.J., Shandarin S.F., Suto Y., 1996, preprint
 Mo H.J., Buchert T., 1990, Astron. Astrophys. 234, 5
 Moutarde F., Alimi J.-M., Bouchet F.R., Pellat R., Ramani A., 1991, ApJ 382, 377
 Munshi D., Sahni V., Starobinsky A.A., 1994, ApJ 436, 517
 Sugino-hara T., Suto Y., Bouchet F.R., Hernquist L., 1991, ApJ Suppl 75, 631
 Suisalu I., Saar E., 1996, MNRAS, submitted
 Weiß A.G., Buchert T., 1993, Astron. Astrophys. 274, 1
 Weiß A.G., Gottlöber S., Buchert T., 1996, MNRAS 278, 953
 Zel’dovich Ya.B., 1970, Astron. Astrophys. 5, 84
 Zel’dovich Ya.B., 1973, Astrophysics 6, 164

Figure Captions

Figure 1a: Central slices of the density field (64^3 trajectories collected into a 64^3 pixel grid) as predicted by the PM-Code (top), Tree-Code (middle) and AP³M-Code (bottom panel) at expansion factors $a = 3.71$ (left) and $a = 5.37$ (right).

Figure 1b: Cross-correlation coefficient and phase angle accuracy are depicted for some evolution stages; the code of reference was AP³M. Full lines mark the cross-correlation with the Tree-Code, dotted lines that with the PM-code. The power-spectrum is also shown: full line: AP³M-code, dotted line: tree-code, dashed line: PM-code.

Figure 2a: The STA mechanism (Model I). The r.m.s. density contrast as a function of the expansion factor is plotted. The numerical result is shown as a full line, 3rd order as a dotted line, 2nd order as a dashed line and 1st order as a dashed-dotted line. The best optimization results are obtained when the numerical r.m.s. density contrast is equal to the corresponding value of the Lagrangian schemes.

Figure 2b: The FTA mechanism (Model I). The r.m.s. density contrast as a function of the expansion factor is plotted. The numerical result is shown as a full line, 3rd order as a dotted line, 2nd order as a dashed line and 1st order as a dashed-dotted line.

Figure 4a: The combination of STA and FTA (Model I, 2nd order). The approximation error as a function of the expansion factor is plotted. STA and FTA optimized: full line, without optimization: dotted line.

Figure 4b: The validity regions of STA and FTA (Model II). The r.m.s. density contrast as a function of the expansion factor is plotted. The numerical result is shown as a full line, 3rd order as a dotted line, 2nd order as a dashed line and 1st order as a dashed-dotted line.

Figure 5: The absolute error in the magnitudes of the cross-correlation coefficient (upper), the power-spectrum (middle) and the phases (lower row) between the numerical result at time a_{num} and Model I is depicted as a function of a ; 3rd order is shown as a full line, 2nd order as a dotted line and 1st order as a dashed line.

Figure 6: The mean quadratic error in the cross-correlation coefficient (top row), the power-spectrum (middle row) and the phase-angle (bottom row) between Model II and the AP³M simulation is shown as a function of the density contrast of the numerical simulation for the third-order (first column), second-order (second column) and the first-order approximation (third column). Dotted lines mark the formal comparison at the same expansion factor, full lines mark the comparison with the “optimally time-shifted” approximations.

Figure 7: The cross-correlation coefficient between the numerical result at time a_{num} and Model I at the same expansion factor (left panels) and at the optimally shifted time (right panels) is depicted as a function of σ_ρ ; 3rd order is shown as a

full line, 2nd order as a dotted line and 1st order as a dashed line.

Figure 8: The power-spectrum of the numerical result at time a_{num} and Model II at the same expansion factor (left panels) and at the optimally shifted time (right panels) is depicted as a function of wave number; the numerical result is shown as a full line, 3rd order as a dotted line, 2nd order as a dashed line and 1st order as a dashed-dotted line.

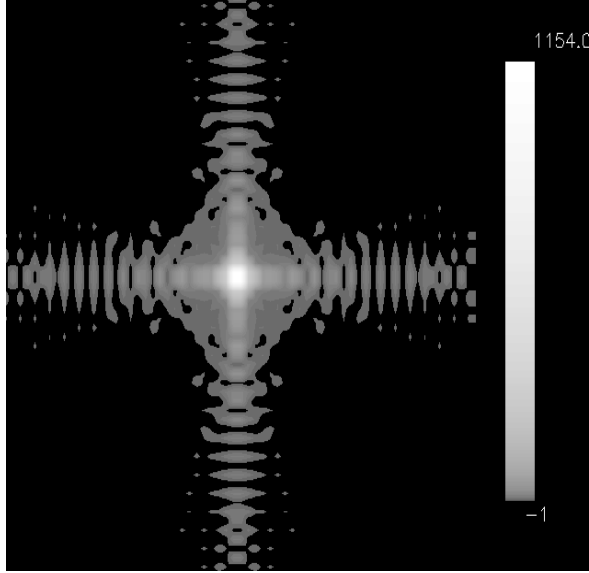
Figure 9: The density contrast of the numerical result at time a_{num} and Model I at the same expansion factor (left panels) and at the optimally shifted time (right panels) is depicted as a function of smoothing scale (in grid units); the numerical result is shown as a full line, 3rd order as a dotted line, 2nd order as a dashed line and 1st order as a dashed-dotted line. It is obvious that the mechanism of STA results in the adaptation of the r.m.s. density contrast.

Figure 10: The phase-error between the numerical result at time a_{num} and Model I at the same expansion factor (left panels) and at the optimally shifted time (right panels) is depicted as a function of wavenumber; 3rd order is shown as a full line, 2nd order as a dotted line and 1st order as a dashed line.

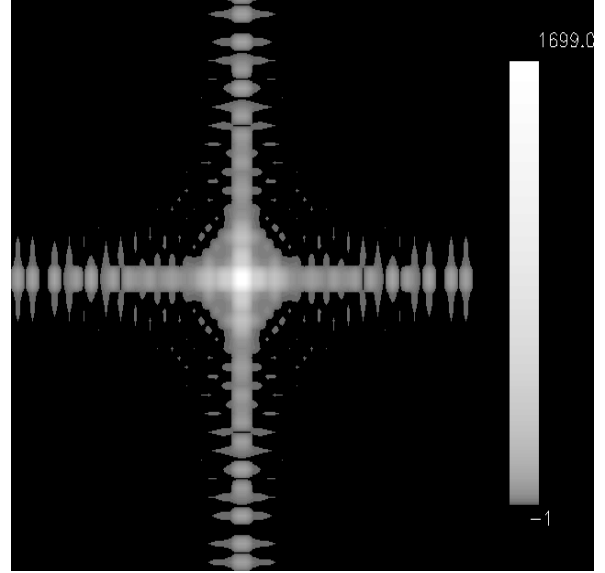
Figure 11a: The approximation error (Model I) is plotted as a function of the expansion factor for FTA and for different numerical expansion factors: The minimum at the expansion factor of shell-crossing for all examined stages can be seen. In the left panels the approximation error for the cross-correlation coefficient (increasing order from top to bottom) and in the right panels the same situation for the relative phase error are shown. The different lines belong to the different initial stages in the range from 3.71 to 6.80.

Figure 11b: Same as Figure 11a, but for Model II.

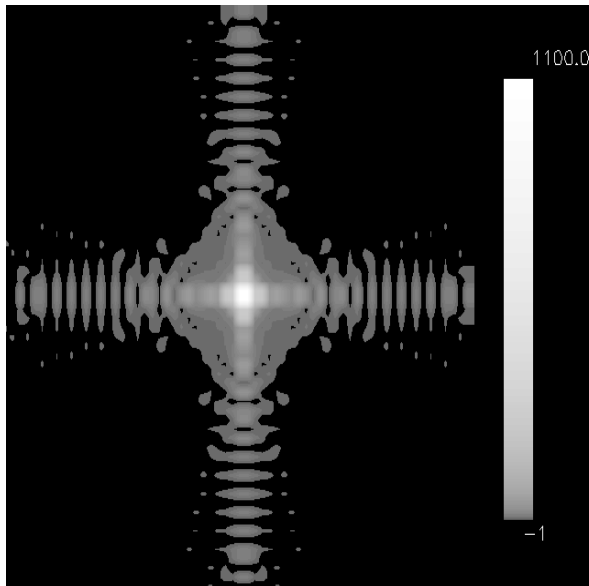
Figure 12: Central slices of the density field for $a_{num} = 3.07$ in Model I (64^3 trajectories collected into a 64^3 pixel grid) as predicted by the AP³M-Code (top left) in comparison with the STA-optimized 3rd order (top right), the STA-optimized 2nd order (middle left), the STA-optimized 1st order (middle right) and the unoptimized 2nd and 1st orders (bottom left and right respectively).



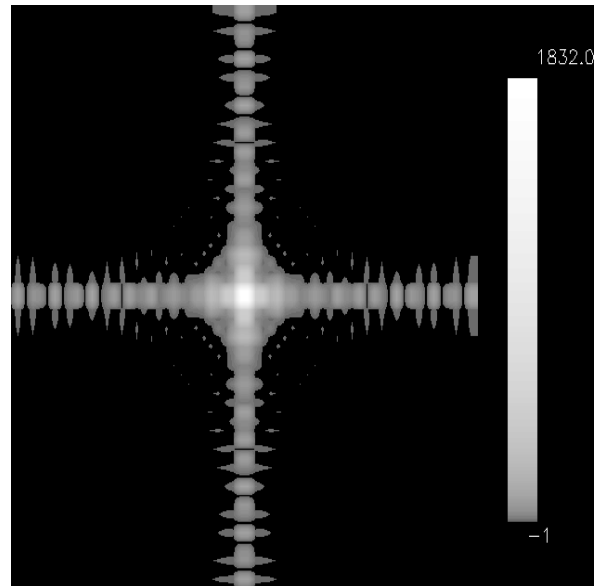
$a=3.71$ (PM-Code)



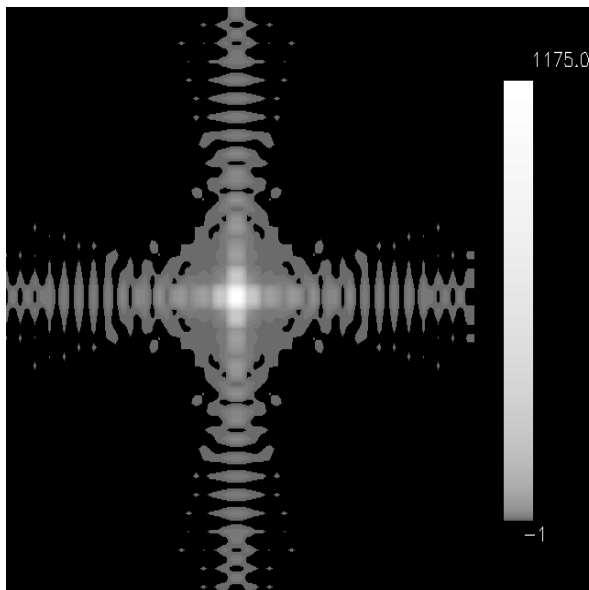
$a=5.37$ (PM-Code)



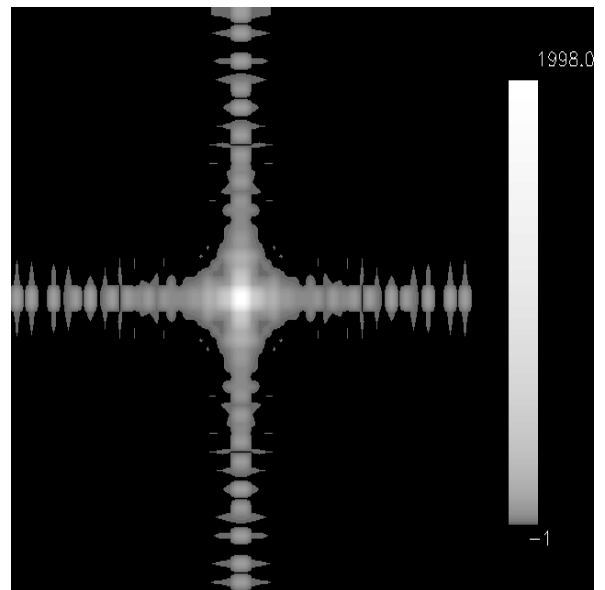
$a=3.71$ (Tree-Code)



$a=5.37$ (Tree-Code)

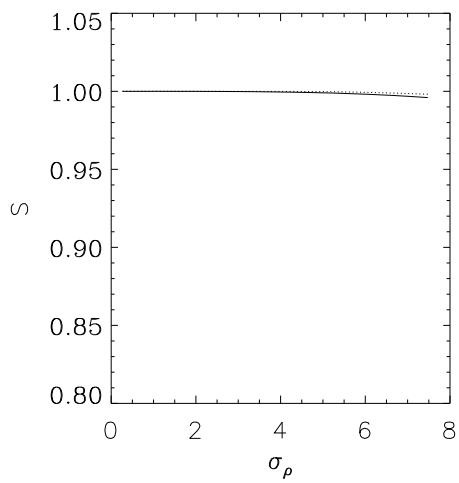


$a=3.71$ (AP³M -Code)

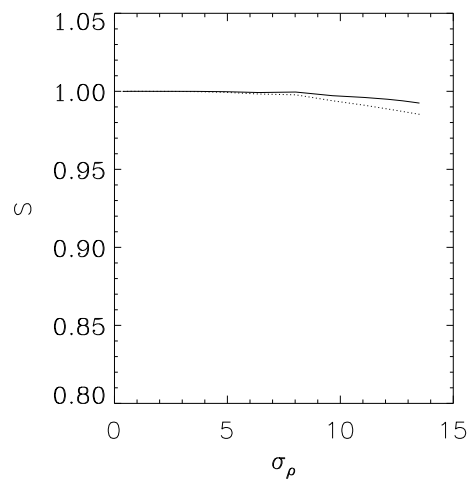


$a=5.37$ (AP³M -Code)

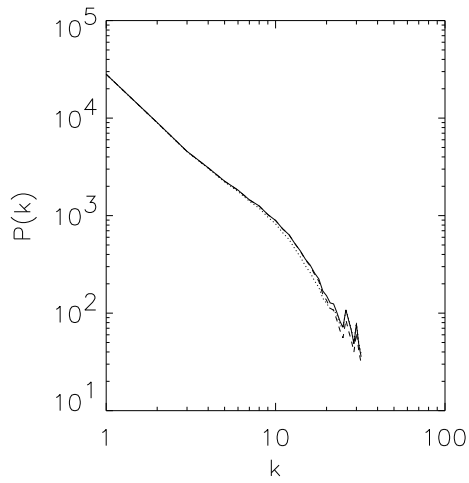
Figure 1a



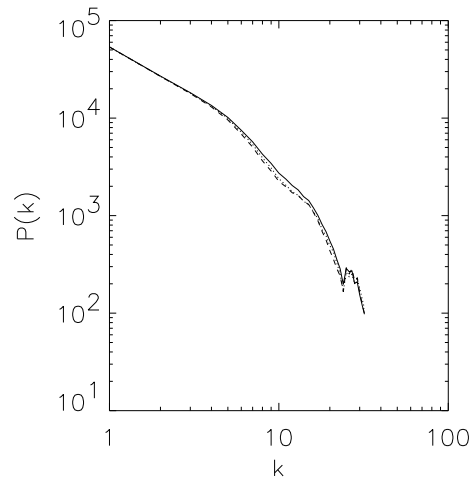
Cross correlation coefficient, $a = 3.71$



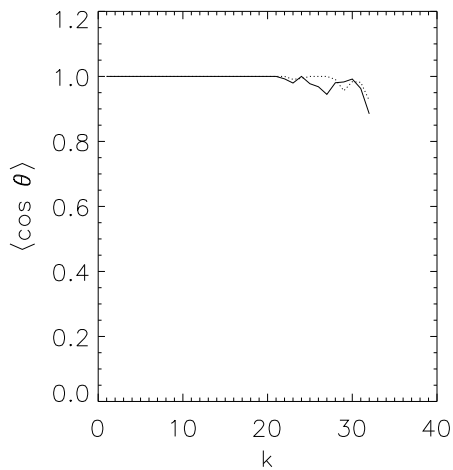
Cross correlation coefficient, $a = 5.37$



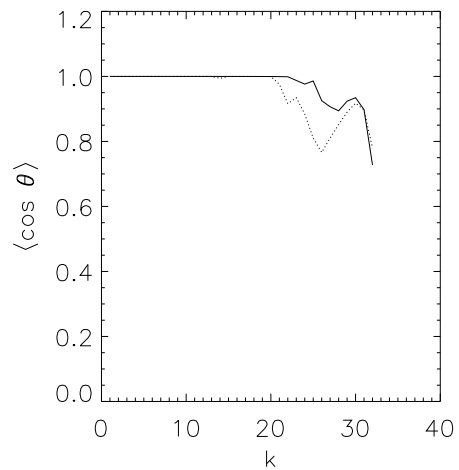
Power-Spectrum, $a = 3.71$



Power-Spectrum, $a = 5.37$



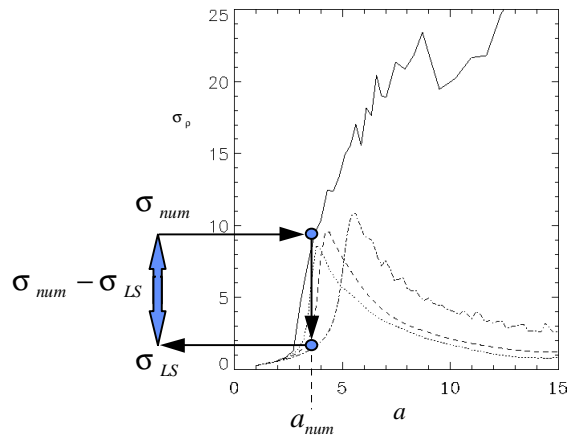
Relative phase error, $a = 3.71$



Relative phase error, $a = 5.37$

Figure 1b

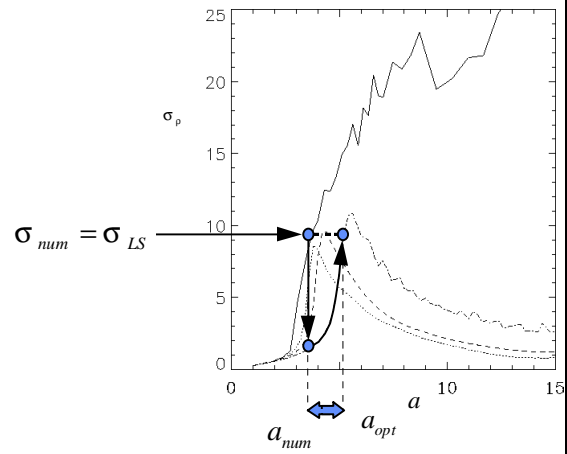
Conventional Optimization Methods



- a_{num} remains constant during the optimization
- measure for the resulting inaccuracy:

$$\sigma_{num} - \sigma_{LS}$$

Shifted - Time Approximation



- STA - shift amount: $a_{opt} - a_{num}$
- optimal results with $\sigma_{num} = \sigma_{LS}$

Figure 2a

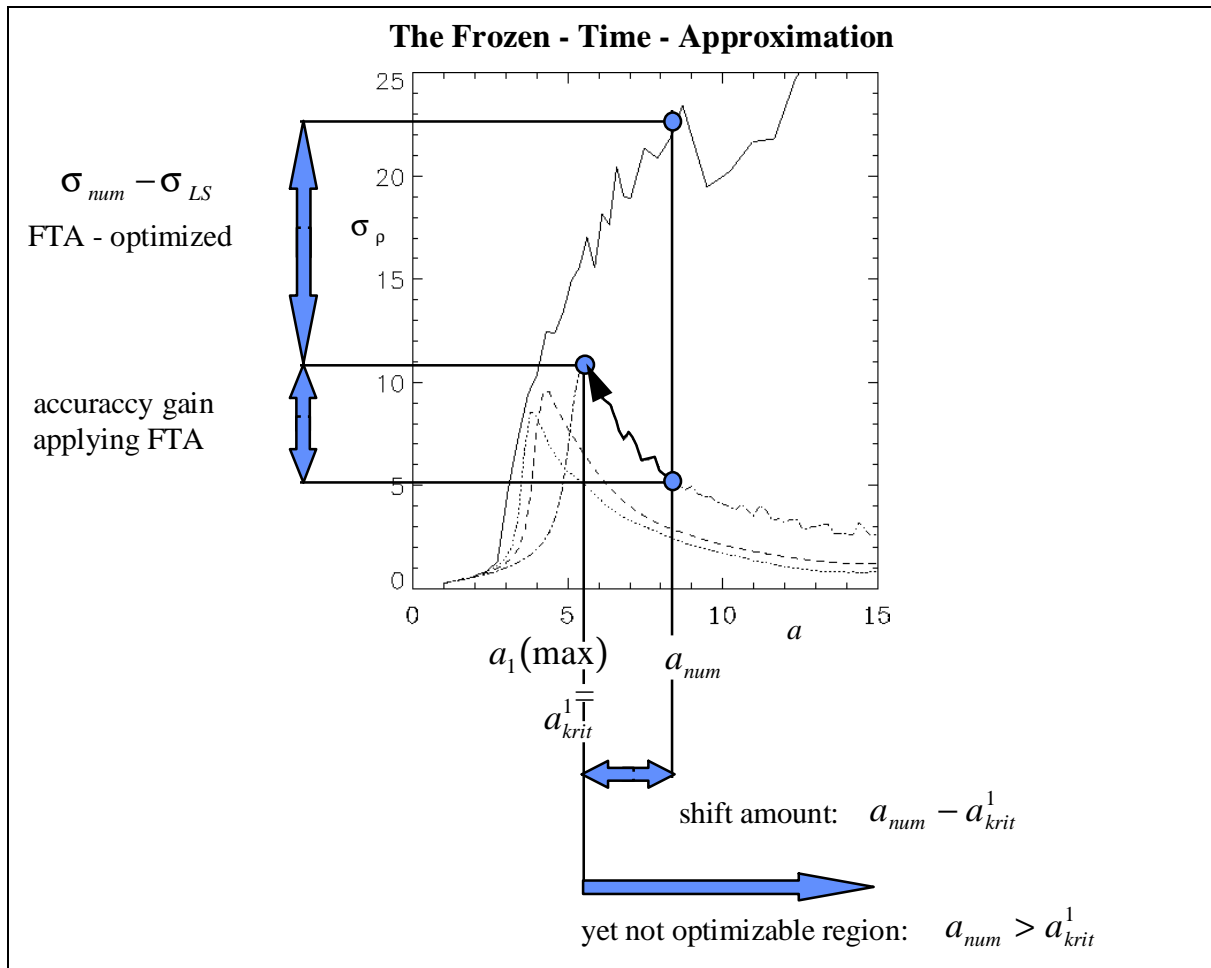


Figure 2b

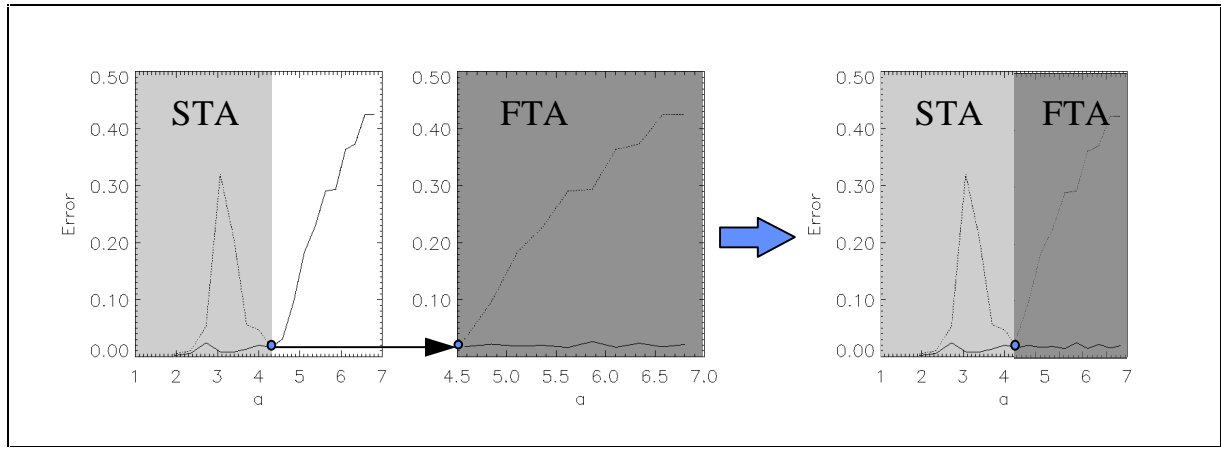


Figure 4a

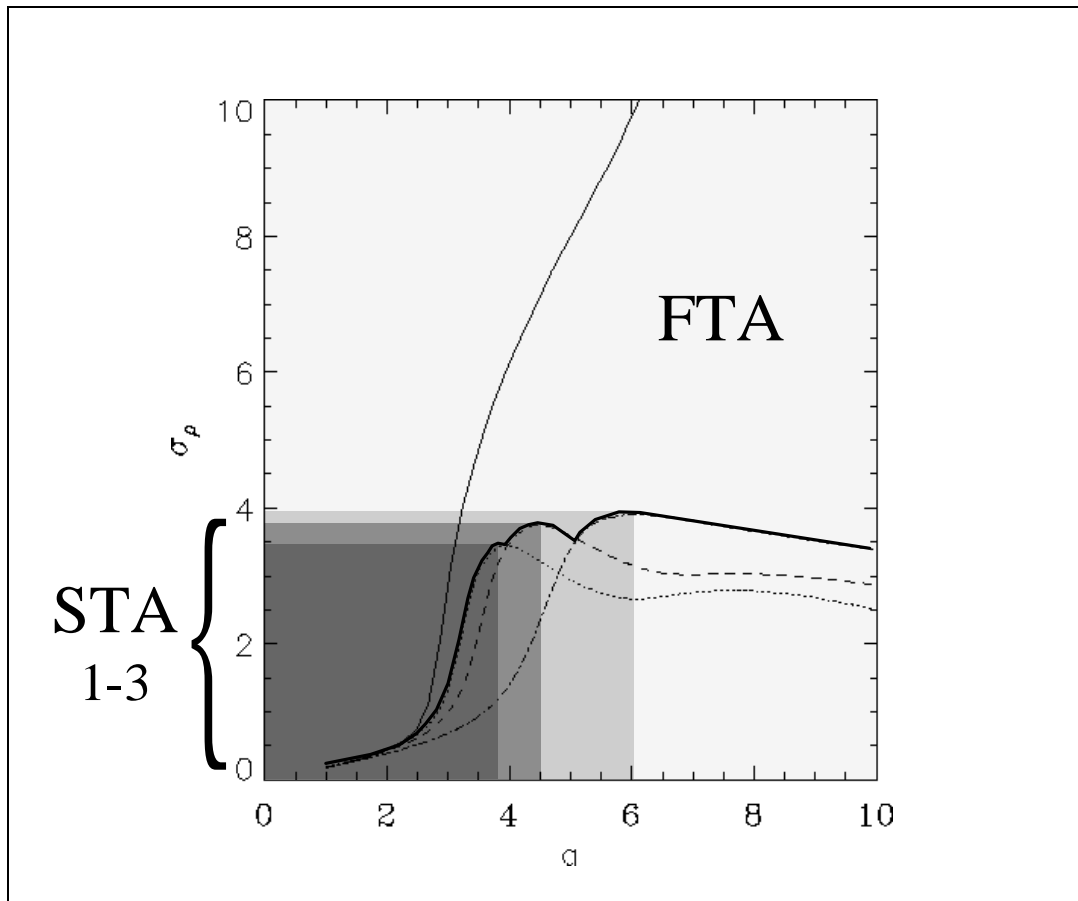


Figure 4b

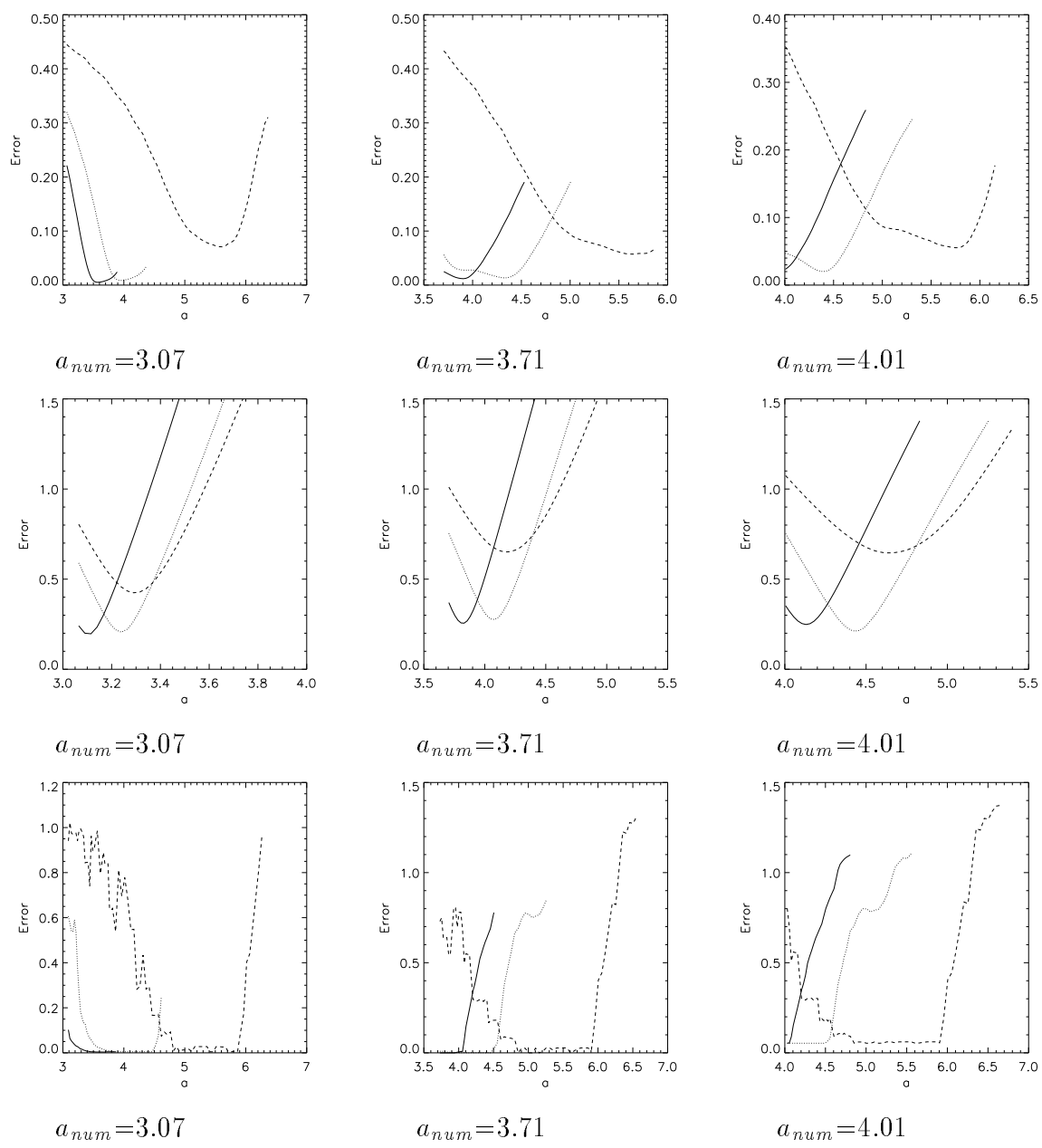


Figure 5

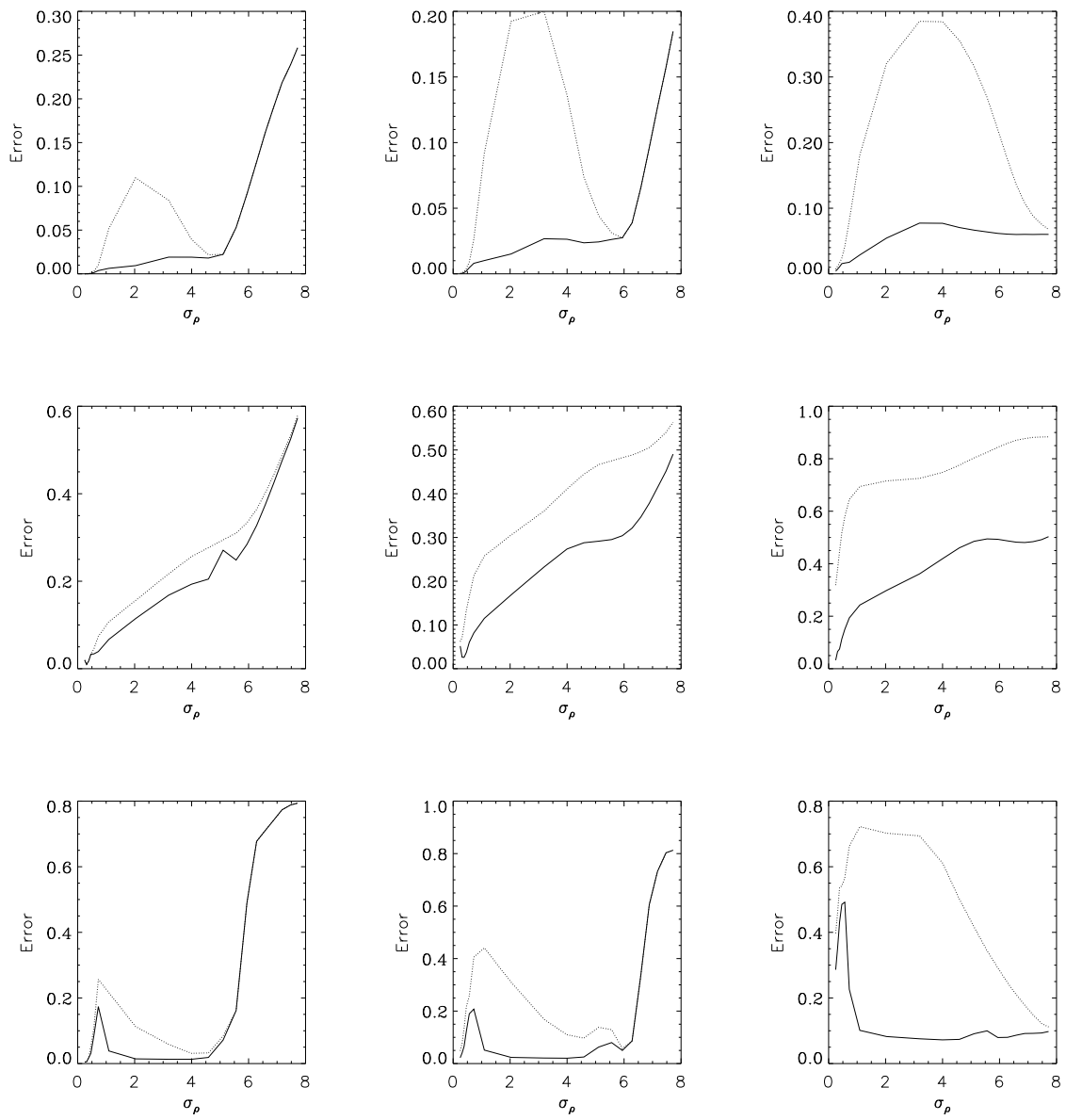
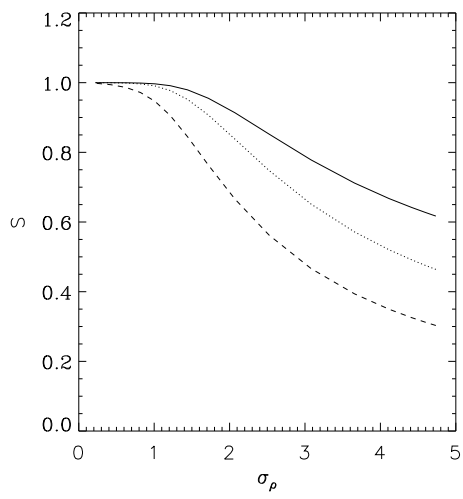
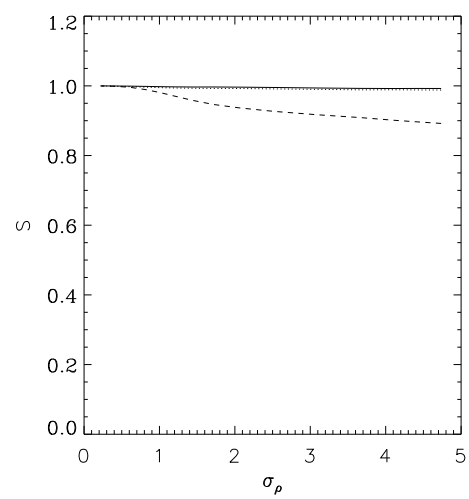


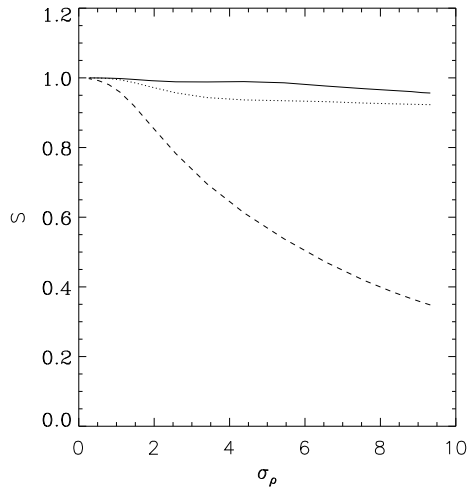
Figure 6



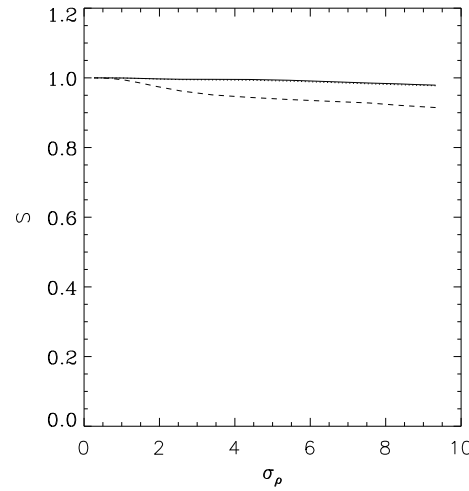
$a_{num} = 3.07$
 $(\sigma_{num} = 4.785)$



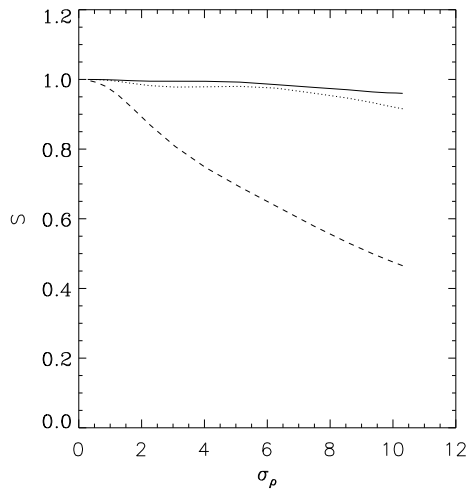
optimally time-shifted models
 $a_{num} = 3.07$



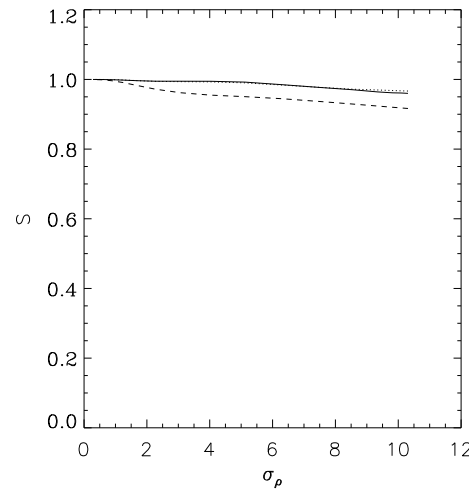
$a_{num} = 3.71$
 $(\sigma_{num} = 9.402)$



optimally time-shifted models
 $a_{num} = 3.71$

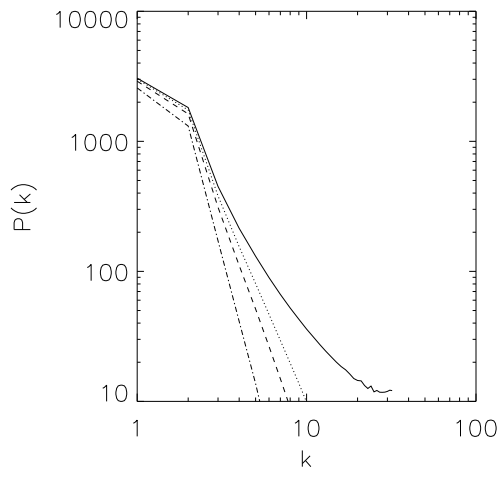


$a_{num} = 4.01$
 $(\sigma_{num} = 10.383)$

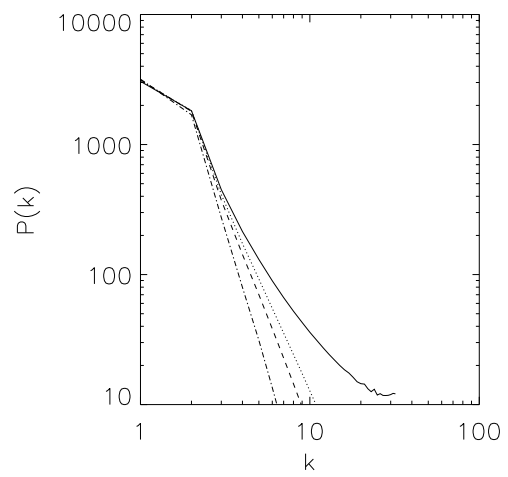


optimally time-shifted models
 $a_{num} = 4.01$

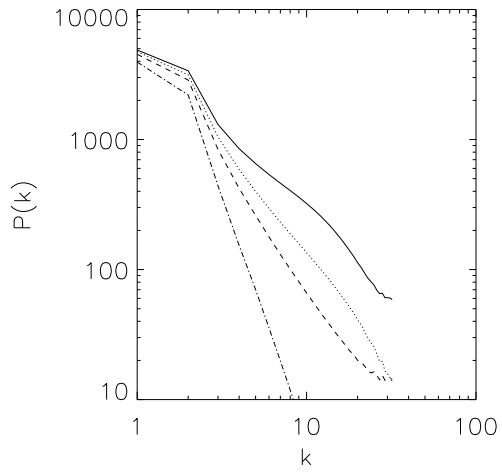
Figure 7



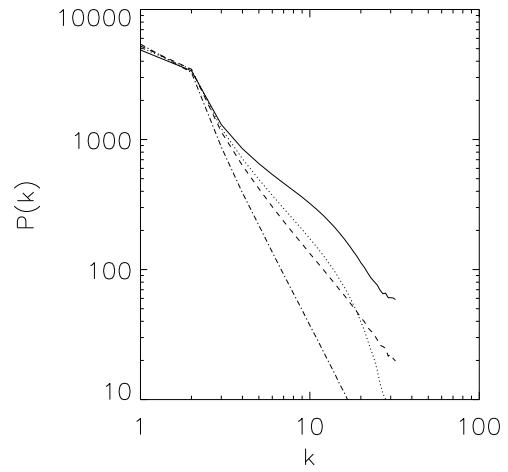
$a_{num} = 2.86$
 $(\sigma_{num} = 2.033)$



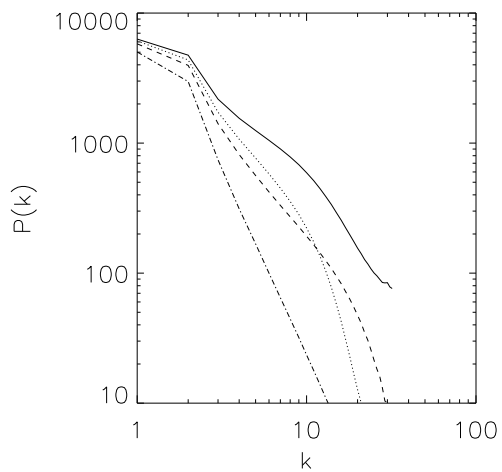
optimally time-shifted models
 $a_{num} = 2.86$



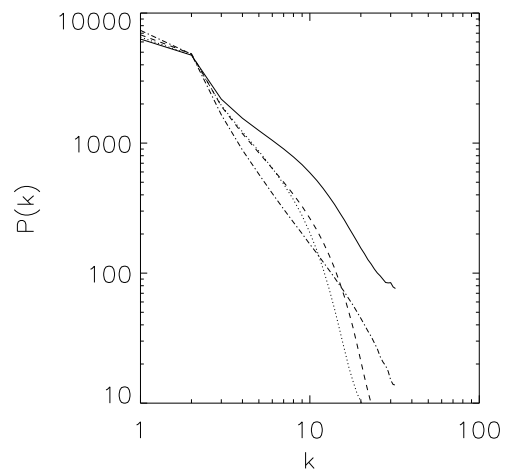
$a_{num} = 3.58$
 $(\sigma_{num} = 5.106)$



optimally time-shifted models
 $a_{num} = 3.58$

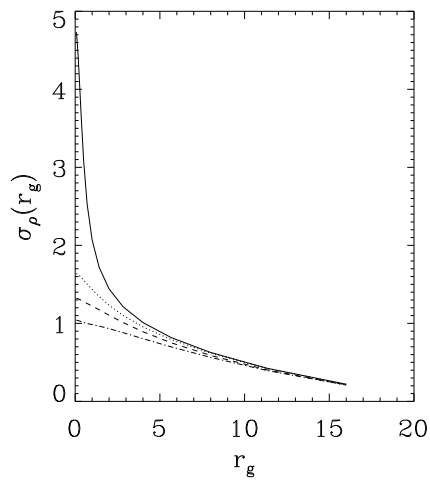


$a_{num} = 4.07$
 $(\sigma_{num} = 6.281)$

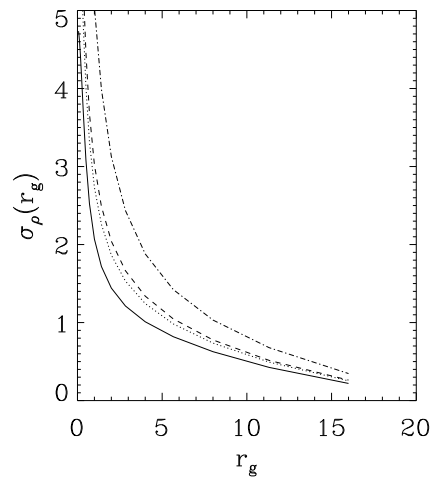


optimally time-shifted models
 $a_{num} = 4.07$

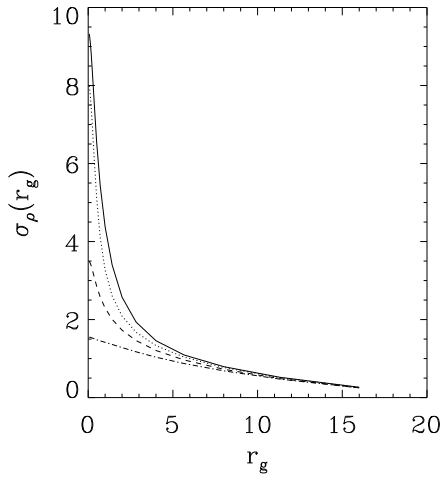
Figure 8



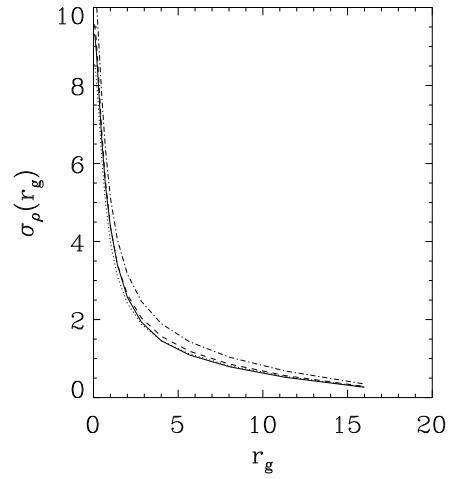
$a_{num}=3.07$
 $(\sigma_{num}=4.785)$



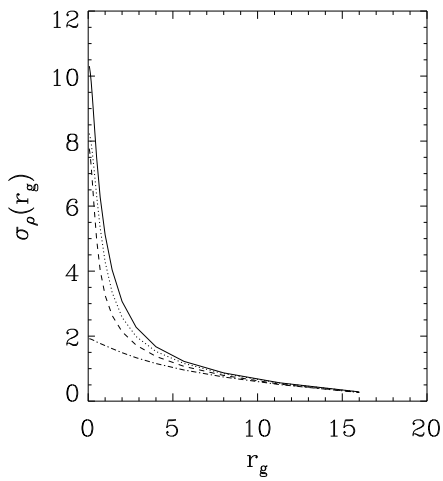
optimally time-shifted models
 $a_{num}=3.07$



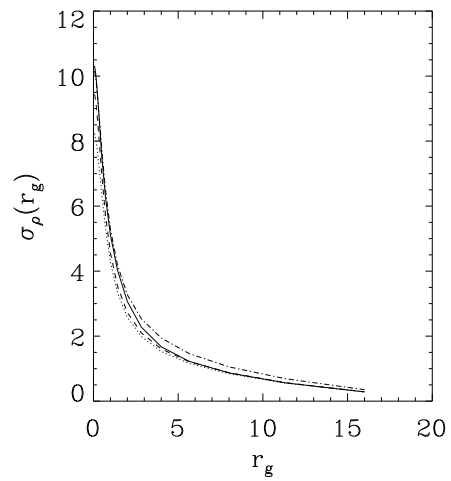
$a_{num}=3.71$
 $(\sigma_{num}=9.402)$



optimally time-shifted models
 $a_{num}=3.71$

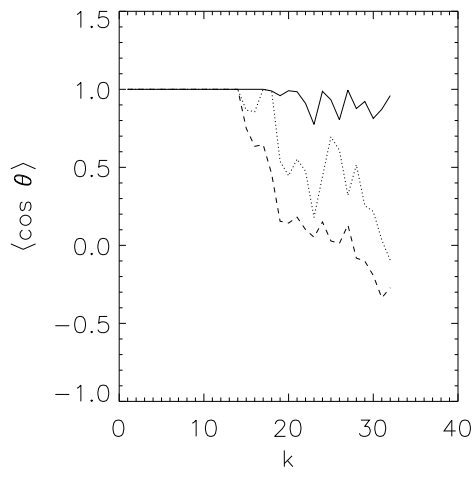


$a_{num}=4.01$
 $(\sigma_{num}=10.383)$

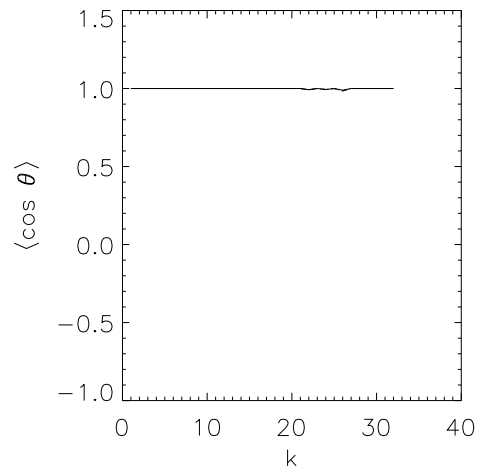


optimally time-shifted models
 $a_{num}=4.01$

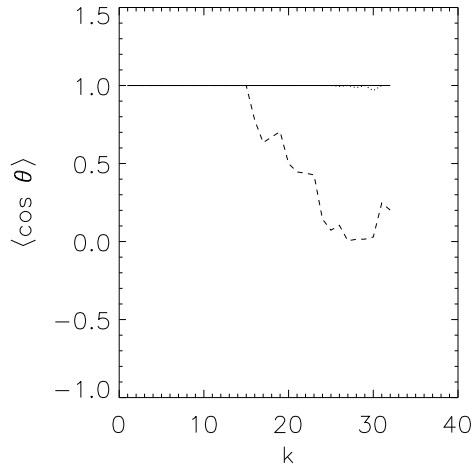
Figure 9



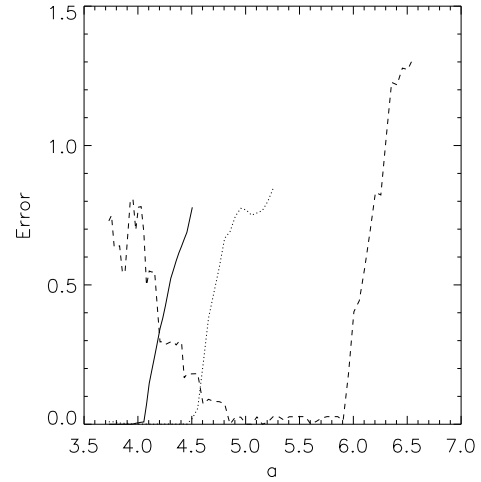
$a_{num} = 3.07$
 $(\sigma_{num} = 4.785)$



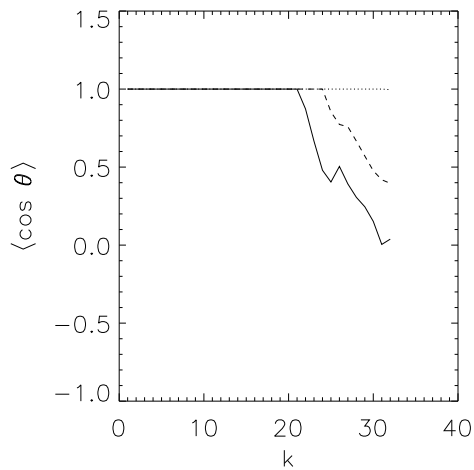
optimally time-shifted models
 $a_{num} = 3.07$



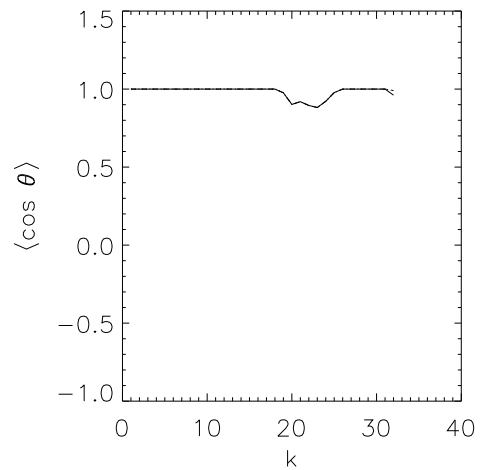
$a_{num} = 3.71$
 $(\sigma_{num} = 9.402)$



optimally time-shifted models
 $a_{num} = 3.71$

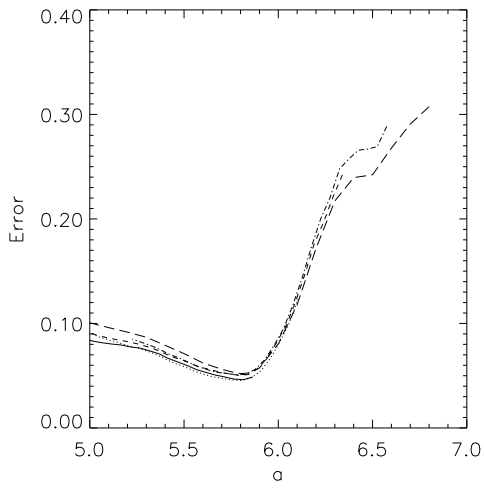


$a_{num} = 4.01$
 $(\sigma_{num} = 10.383)$

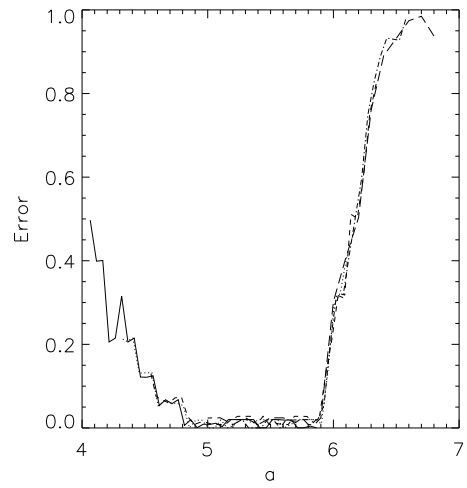


optimally time-shifted models
 $a_{num} = 4.01$

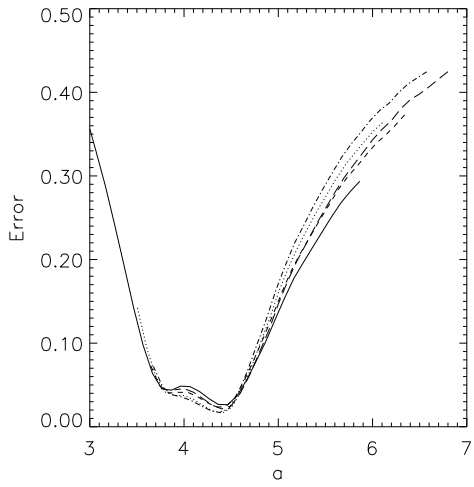
Figure 10



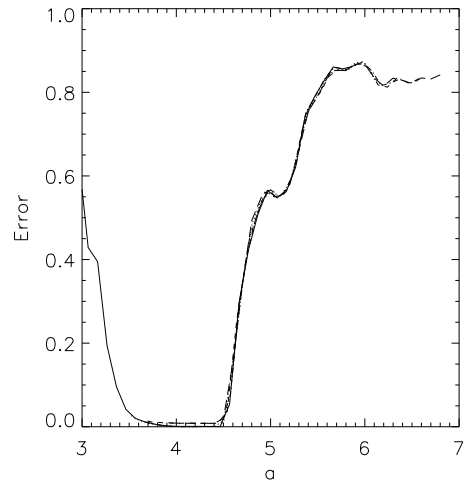
Cross correlation, 1. order



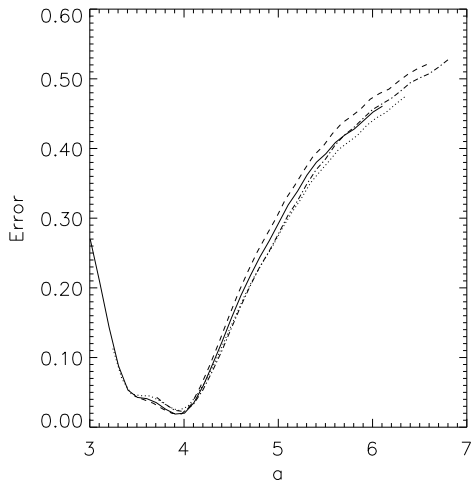
Relative phase error, 1. order



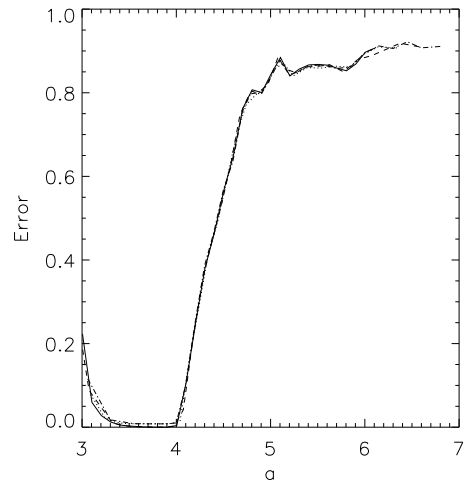
Cross correlation, 2. order



Relative phase error, 2. order

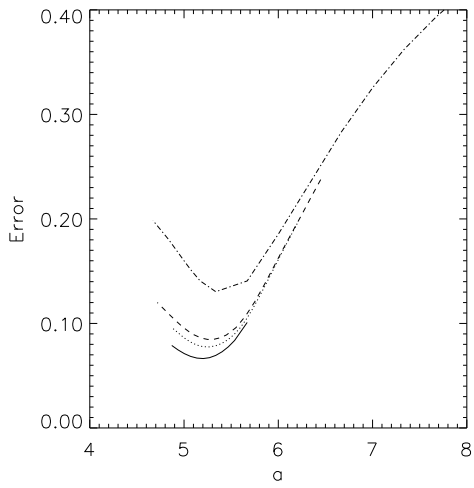


Cross correlation, 3. order

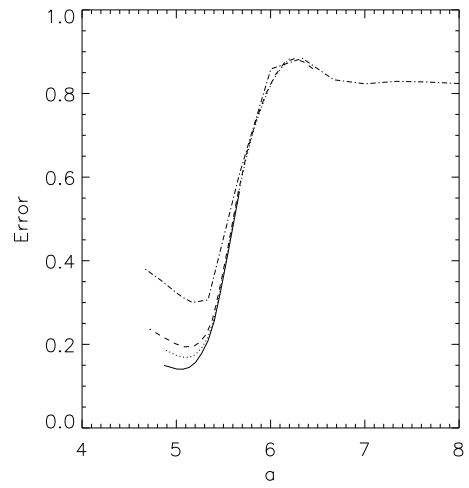


Relative phase error, 3. order

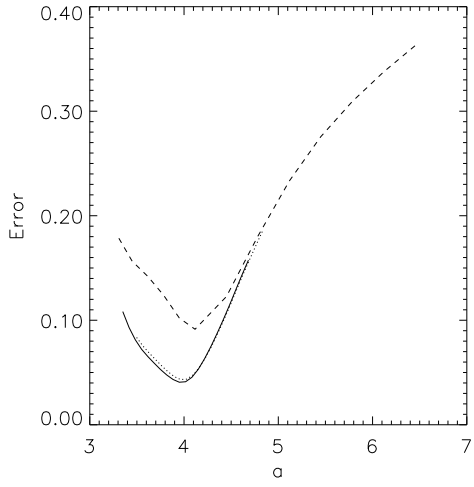
Figure 11a



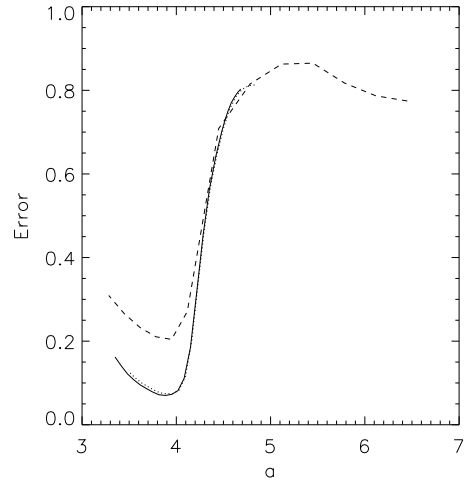
Cross correlation, 1. order



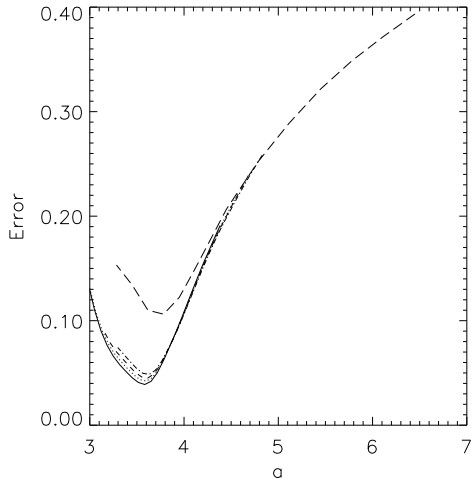
Relative phase error, 1. order



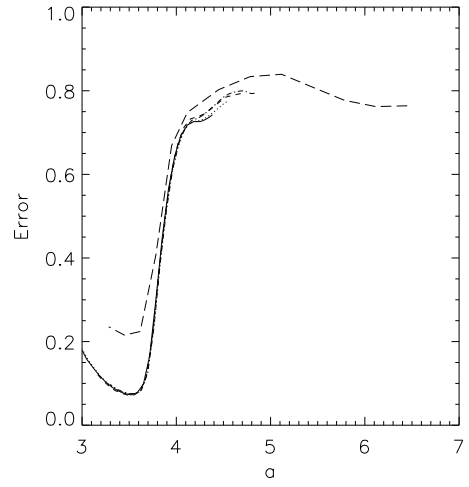
Cross correlation, 2. order



Relative phase error, 2. order

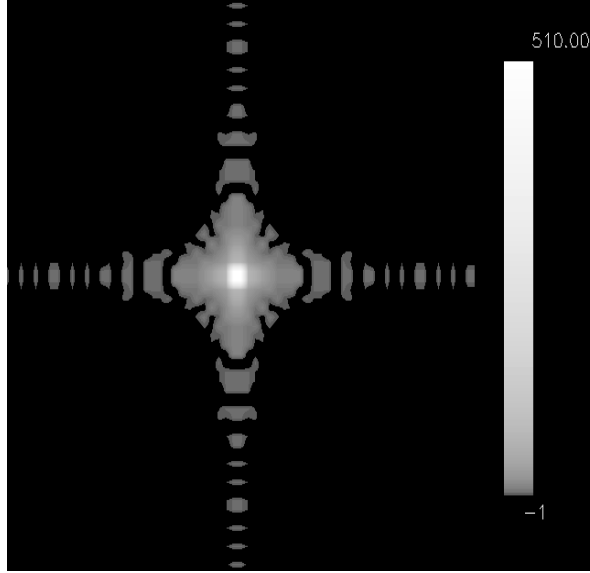


Cross correlation, 3. order

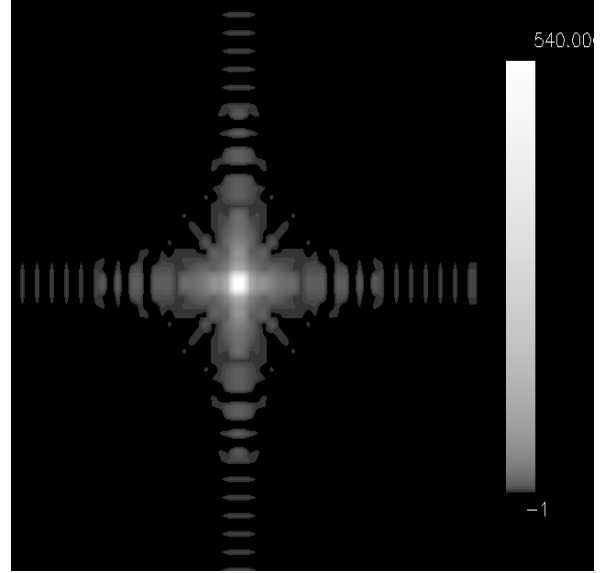


Relative phase error, 3. order

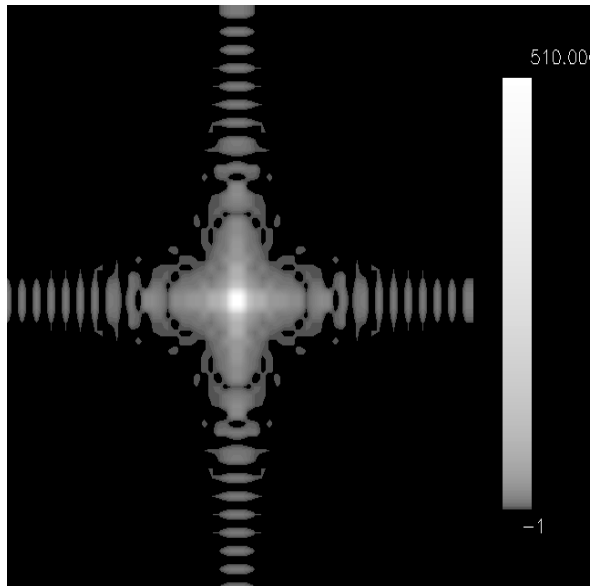
Figure 11b



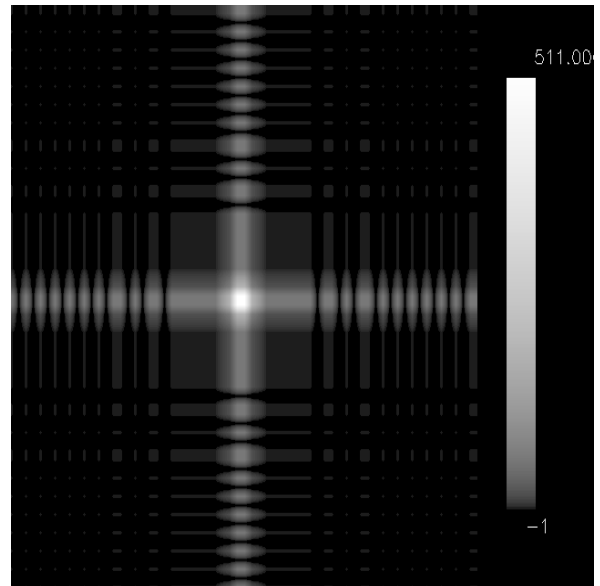
$a=3.07$, AP³M-Code



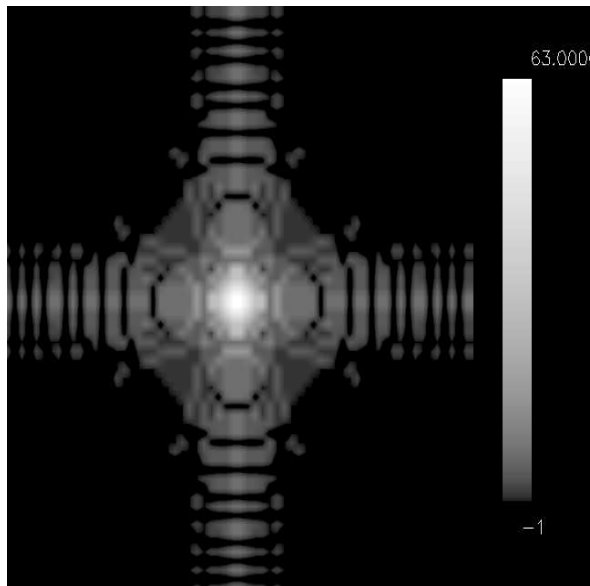
$a=3.48$, optimized 3rd order



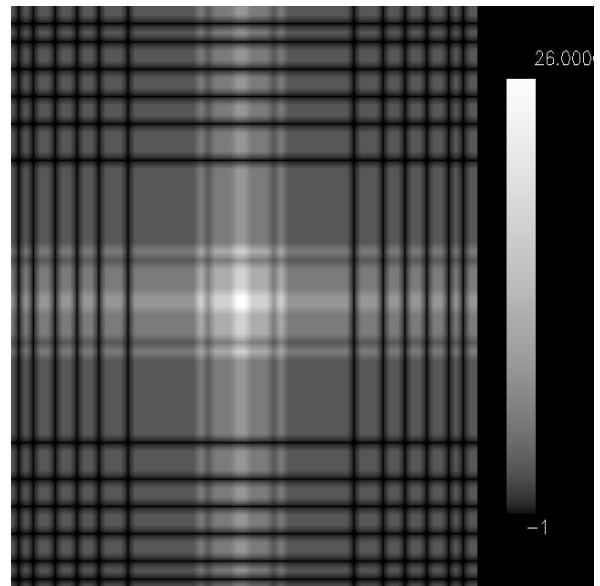
$a=3.78$, optimized 2nd order



$a=5.00$, optimized 1st order



$a=3.07$, unoptimized 2nd order



$a=3.07$, unoptimized 1st order

Figure 12